(article starts on next page)

Contents lists available at ScienceDirect

Tribology International

Fluxes in a full-flooded lubricated Tapered Roller Bearing: Particle Image Velocimetry measurements and Computational Fluid Dynamics simulations

Lorenzo Maccioni [a], Valery G. Chernoray [b], Franco Concli [a,*]

[a] *Free University of Bozen-Bolzano, Faculty of Engineering, Piazza Università 1, 39100, Bolzano, Italy*
[b] *Chalmers University of Technology, Mechanics and Maritime Sciences, 41259 Gothenburg, Sweden*

ARTICLE INFO

ABSTRACT

The acquisition of complex fluxes inside a Tapered Roller Bearing (TRB) via Particle Image Velocimetry (PIV) is an experimental challenge. This can be successfully performed by exploiting a special test rig having the outer ring manufactured with sapphire. In the present paper, the velocity field in the region between cage, rollers and outer race have been captured via PIV in a fully flooded lubricated TRB. The experimental conditions have been reproduced numerically via Computational Fluid Dynamics (CFD). The comparison of PIV results with CFD ones showed excellent consistency. It has been observed that, in the target domain, the tangential velocity of the lubricant is greater than those of the cage. In addition, in the proximity of the edges of the rollers, squeezing effects due to high gradients of pressure have been recorded. The distribution of flow rates due to the pumping effect in different regions of the TRB have been estimated.

1. Introduction

In recent years, the development of Computational Fluid Dynamics (CFD) models for studying rolling-element bearings lubrication has grown in interest in research [1]. For example, in [2] the oil-bath lubrication of specific ball and roller bearings has been studied through CFD. Peterson et al. [3] performed a CFD investigation of lubricant fluxes in deep groove ball bearings. Zhu et al. [4] analyzed the lubricant flows in double-row Tapered Roller Bearings (TRBs). Maccioni et al. [5,6] investigated and simulated a full-flooded lubricated TRB in presence of aerated lubricant.

CFD models allow estimating both lubricant fluxes and load-independent Power Losses (P_{LB_0}), i.e. power losses due to inertial and viscous effects of fluids on moving mechanical components. For instance, Raju et al. [7] estimated via CFD lubricant flows in needle roller bearings. Adeniyi et al. [8] developed a CFD model to study the lubricant fluxes in the proximity of an aeroengine bearing. Eventually, Wu et al. [9] investigated oil fluxes in jet cooling ball bearings. On the other hand, P_{LB_0} have been estimated through CFD in oil-jet lubricated ball bearings in [10,11] and in cylindrical roller bearings in [12,13].

In this context, where more and more new CFD models are developed by the scientific community, their experimental validation plays a key role in the progress of this research field [1]. Within this frame of reference, Particle Image Velocimetry (PIV) measurements are becoming increasingly popular to study flows in various mechanical systems [5,14]. Indeed, velocity fields can be measured via PIV paving

the way for the validation of the CFD results [6,14]. For example, PIV studies have been conducted on gears with the aim of studying lubricant flows in [14], and the results have been compared with the numerical ones acquired by [15]. Similar studies on gears have been performed in [16] exploiting Smooth Particle Hydrodynamics (SPH). The P_{LB_0} due to windage, i.e. power losses due to the inertial and viscous effects of air on high-speed gears, have been studied numerically (via CFD) and experimentally (via PIV) in [17]. PIV measurements and CFD results have been compared in [18] for a thrust bearing. The development of CFD models and the related validation via PIV was also conducted for a TRB in [5,6] and for a ball bearing in [19,20].

In the present paper, experimental PIV measurements and numerical CFD simulations have proved to be two useful and complementary approaches for studying flows within a TRB. The first part of the paper is focused on the description of the experimental campaign aimed to measure the flows inside a TRB for different operating conditions. This involves test rig design, instrumentation set up and data processing. The data experimentally acquired, in terms of fluxes and velocity fields inside a TRB, paved the way for the validation of the CFD numerical models of the lubrication inside a TRB. Therefore, in the second part of the paper, the CFD models of the selected TRB are presented and the results compared with the PIV ones.

In Section 2, the background of this study is presented. In particular, the activities aimed at obtaining experimental data on the fluid

---

* Corresponding author.
  E-mail address: franco.concli@unibz.it (F. Concli).

behavior inside or in the proximity of rolling-element bearings are described (Section 2.1). These measurements rely on optical systems. Moreover, in Section 2.2, a state of the art of experimental studies involving lubrication of TRBs can be found. In Section 3, details of the developed test rig and its operation are presented. In addition, the setup of the PIV instrumentation and the experimental approach used to conduct the measurements are explained. In Section 4, the numerical modeling techniques are presented. The CFD and PIV results are illustrated, compared, and discussed in Section 5. Conclusions can be found in Section 6.

2. Background

2.1. Experimental studies applying optical measurements in rolling-element bearing lubrication

In Yan et al. [19], PIV measurements have been performed inside the cavity of an angular contact ball bearing to study the main air flows and the vortex distribution. To execute PIV measurements from a radial perspective, the main components (i.e., cage, outer ring, and external case) have been realized in Perspex. Through this transparent plastic, it was possible to optically access the bearing. The cross-correlation analysis of images acquired with high-frequency cameras allows reconstructing the velocity field in a radial cross-section of the bearing (section plane including the bearing axis). In this way, it was possible to observe specific vortices that occur on both sides of the rolling element. More specifically, the scholars observed that the intensity of these vortices increases as the rotational speed of the bearing increases. However, due to the poor mechanical properties of the Perspex, a maximum rotational speed of 1300 min^{-1} was reached.

The test rig originally developed by Russell et al. [21], for the study of friction between the cage and the ball of a deep groove ball bearing, has been adapted by Aamer et al. [20] to perform optical measurements. The test rig was designed to control directly the rotational speed of the ball (12 mm diameter) in a real scale bearing sector (without the outer ring). The test rig allows to control the relative position of the cage to the rotating ball by measuring the resulting torque on the rolling element. In the above-mentioned work, the cage, which had zero velocity in the absolute reference system, has been manufactured in acrylic to allow a clear view on the cage-ball gap. The outer ring has not been mounted in order to allow optical access. The measurements have been performed for different rotational speed of the ball (300 min^{-1}, 600 min^{-1}, and 1200 min^{-1}) and for different relative positions between cage and ball. The results have been compared to those obtained via multiphase CFD modeling. The comparison highlighted good agreement and revealed that the surface tension coefficient has a relevant influence on the oil distributions. Moreover, Aamer et al. [20] were able to observe that decreasing the cage-ball gap, the air entrapment within the pocket tend to increase. In addition, the scholars observed that increasing the ball speed, the lubricant striations on the ball became more numerous (and smaller). However, in their study, the effects of the apparent forces due to the actual movement of the ball, cage, and inner ring were not analyzed as well as the effect of the outer ring. Eventually, only the distribution of flows was tracked (and not their velocities).

In Noda et al. [22,23], X-ray computed tomography has been exploited to map the grease distribution in a ball bearing. In these studies, metal components were not exploited since the high intensity of X-rays required for metals does not allow achieving a sufficient resolution to map the grease distribution. Therefore, a fluoro-resin carbon fiber composite has been used to manufacture the inner ring, the outer ring and the cage; balls have been realized in glass. The X-ray computed tomography allowed to exploit a maximum speed of the shaft of 600 min^{-1} based on its maximum frequency acquisition capability. The experiments reveal that the grease, at that specific rotational speed, tends to accumulate in specific volumes of the bearing. Moreover,

through this study, it has been possible to observe the transition of the grease from the circulation condition to the channeling one [24] through the mixture distribution of urea and barium-based greases (having different properties in terms of X-ray absorption).

The behavior of lubricant in the proximity of the bearings has been assessed qualitatively using photographs in [9,25,26]. An experimental and numerical study of the splashing of ball bearings with different cages is presented in [25,26]. By observing the oil flow at a macro level with a transparent surface, it has been possible to distinguish between the splashing patterns induced by different cage geometries. A CFD study and an experimental campaign were conducted in [9] to investigate the lubricant flows and temperature distribution within a jet-lubricated ball bearing. In this work, the scholars observed fluid fields by acquiring images from an axial perspective. It has been shown that the oil fraction around the nozzle is higher than in other areas. This information was useful in determining the number and position of nozzles ensuring a proper lubrication. The axial perspective, has been exploited also in [26] with the aim of investigating the shedding mechanisms in proximity of an aero-engine ball bearing. The scholars individuated three different oil break-up mechanisms at different speed ranges (between 1000–7000 min^{-1}), i.e. direct-drop formation for low speeds, ligament breakup for medium speed, and sheet disintegration for high speed.

In [27], the oil flows have been investigated in an angular contact ball bearing using Bubble Image Velocimetry (BIV) exploiting a counter-rotating test rig. BIV is a variation of the PIV technique, where bubbles are directly used as tracer particles for quantification of flow velocity. The test rig exploited in the above-mentioned study allows to set into rotation both the outer ring and the inner ring, keeping at the same time the cage stationary. In this way, the scholars, through transparent acrylic cages, were able to capture images with a high-speed camera in a bearing sector. Different cages have been tested up to a rotational speed of the inner ring of 400 min^{-1} to guarantee an appropriate filling level of the oil. The experimental results have been compared with CFD simulations in a stationary reference frame.

Eventually, the droplet generation in an aero-engine bearing chambers has been studied by Gorse et al. [28] through PIV measurements. The realistic conditions have been created in a specific test rig for a cylindrical roller bearing. Using an axial view, the image acquisition and data elaboration revealed a strong influence of the bearing support on droplet generation.

2.2. Theoretical and experimental studies on tapered rolling bearings lubrication

Leibensperger [29] performed a theoretical analysis of the oil flows in a TRB. The developed oil flow model through a TRB is based on boundary layers. The assumption behind the above-mentioned theory is that the oil flows through a TRB can be divided into two regions, i.e. a potential-flow region (where viscous effects are negligible), and a boundary-layer region (where viscous effects are predominant). In the potential-flow region the oil has the same speed of the cage. This lead to the oil to be subjected to a normal acceleration and, therefore, to increase its radial (outward) speed. Then, based on this assumption, in the potential-flow region, the velocity parallel to the surface of the outer race is negligible. Essentially, in the above-mentioned region, the oil-flow is considered subjected to rigid body rotation and viscosity effects are considered negligible. On the other hand, the oil is thrown radially outward, and it reaches the conical surface of the outer ring. Therefore, at that point, the flow direction is changed and a velocity parallel to the cup surface increases. This region, where also axial flows are presents, is the boundary-layer. According to [29], all the axial oil flow occurs only in the boundary layer region. Therefore, the scholar developed an analytical model to calculate the axial flow (due to the pumping effect) at different operating condition and for different bearing dimensions.

In [30] an analytic torque model of TRBs is presented together with experimental results. The analytical model is based on Elasto-Hydrodynamic Lubrication (EHL) theory and micro-macro contact analysis. In the above-mentioned study, the contact surface roughnesses, the EHL film thickness parameters, and thermal EHL effects have been considered. The developed test rig has allowed measuring the torque of the different component of the inner ring (rib, cup race, and conical race) independently.

With the aim of investigating hydraulic P_{LB_0} on a TRB, Liebrecht et al. [31,32] designed a vertical test rig. The test rig allows controlling the level of the oil lubricating the TRB and the rotational speed by measuring the torque on the shaft and the oil temperature. The concept behind the estimation of the P_{LB_0} due to the inertial and viscous effects of the lubricant is to measure the P_{LB_0} in the full-flooded lubrication condition, and in a condition in which the level of lubricant is minimum. The difference between the two conditions is a good estimation of the hydraulic P_{LB_0}. In the above-mentioned study, the P_{LB_0} have been estimated for different rotational speeds (up to 6300 $\min^{-1}$), different oil temperatures (up to 80°C), and different levels of the oil (up to 3 times the width of the TRB). The scholars had noticed foaming in experiments and have tried to develop a numerical model that would consider this physical phenomenon in P_{LB_0} calculation. They fine-tuned a CFD model that considers the variation of oil properties, such as density and viscosity, based on the rotational speed of the shaft. The results of this experimental campaign have been further discussed in [33–37].

More recently, Maccioni et al. [5,6] designed and developed a specific test rig to perform PIV measurements on oil flow inside a TRB. The scholars exploited a sapphire outer ring to have the optical access inside a TRB during its functioning. Through the PIV measurements, the authors have mapped the lubricant velocity field in the cavity between the outer ring and the cage at different rotational speeds (up to 2000 $\min^{-1}$ of the inner ring). As mentioned at the beginning of this section, in this area the pumping effect is expected to be more relevant [29]. During the experimental campaign, the scholar observed that, with increasing the rotational speed, bubbles due to aeration phenomena tend to appear. A similar phenomenon, in terms of foaming, had been observed also by [31,32]. In the study carried out by Maccioni and colleagues [5], it has been possible to observe how the presence of aeration tends to modify the velocity field in the studied volume. In subsequent studies, [6], the scholars developed a CFD model that takes into consideration aeration. This model involves a new solver, implemented in the open-source environment OpenFOAM®, based on the analytical aeration model by Hirt [38]. The numerical results have been compared with the experimental ones. The comparison shows that for low rotational speeds (where aeration can be negligible) standard solvers can be considered appropriate to estimate the velocity field. On the other hand, for high rotational speeds (higher level of aeration), the new solver can provide satisfactory results while standard solvers could not.

Eventually, it is worth mentioning some research involving the study of temperature and heat fluxes in TRB. In particular, Brecher et al. [39] measured temperatures and friction moments in a TRBs lubricated through specific holes drilled in the outer ring. Zhou et al. [40] investigated the temperature field in a double-row TRB. Roshchin [41] developed a criterion to estimate the heat generation in TRBs operating in specific conditions. The scholar claims that the heat generated is equivalent to the total P_{LB_0}.

3. Experimental approach

3.1. Test rig

The test rig exploited in the present research is described in detail in [5,6]. Compared with previous studies, the dynamic behavior of the test rig has been improved (i.e., the level of vibration at high

Table 1
Dimensions of 32312-A bearing.

Symbol	Description	Value	Unit
d	Bore diameter	60	mm
D	Outside diameter	130	mm
B	Total width	48.5	mm
N	Number of rollers	16	–
D_p	Pitch diameter	94.8	mm
d_R	Mean roller diameter	17.4	mm
α	Angle of contact	11	°

rotational speeds has significantly decreased). This was achieved by using a lighter shaft and employing stiffer dampers. In the present work, the geometry related to the TRB 32312-A, manufactured by Schaeffler Technologies GmbH, has been studied. This TRB presents the geometrical characteristics listed in Table 1. The main feature of this test rig is the outer ring made of sapphire that, due to its transparency, allows performing PIV measurements. To improve the surfaces clearness, grinding and polishing operations have been performed, ensuring a geometry of the outer ring that meets the geometrical and dimensional tolerances of the original steel design. The sapphire's hardness is sufficient to avoid scratches or wear in the inner race maintaining its optical properties during the entire test. Therefore, it is possible to load the TRB with the minimum load that ensures the correct kinematics of the rollers, i.e. no-slip condition. Original metallic rollers, cage and inner ring have been exploited in this study.

In Fig. 1, the test rig is shown in its actual assembly together with its CAD model. The working principle of the test rig is the following: the central screw positioned on the bottom of the test rig allows controlling the axial loading of the bearing by deforming the cup springs. Indeed, the compression of the cup springs leads to an axial force that, on the one hand, is conveyed to the outer ring, and on the other hand, is transmitted to the frame by the above-mentioned screw. From the outer ring, this force (up to 5 kN) is transmitted through the rollers to the inner ring, the shaft, the angular contact bearing and, finally, to the frame.

Once the system is preloaded, and thus the kinematic of the various components is ensured, the shaft can be set into rotation. This can be done by the three-phase 2.2 kW electric motor with velocity feedback, controlled by an inverter, coupled with the shaft through a bellows joint.

In this study, the entire test rig was filled with oil. Therefore, the oil level is about three times the axial width of the TRB. The rotation of the various components of the TRB induces a pumping effect. In this regard, the CAD model presented in Fig. 1 shows, with yellow arrows, the main oil paths. The vertical architecture of the test rig provides axis-symmetrical operating conditions in terms of lubricant distribution. Indeed, in this configuration, gravity acts parallelly to the axis of rotation. In Fig. 1, it is possible to notice two different chambers where the lubricant is present: the lower one and the upper one (with respect to the TRB). In each chamber, the oil temperature has been monitored with thermocouples. In addition, in Fig. 1 it is possible no notice six O-rings that prevent oil leakage. Eventually, dampers were introduced to limit vibrations at the base of the test rig. During its operation under full-flooded lubrication, the PIV measurements can be conducted through the specific window that allows the optical access (See Fig. 1).

3.2. Set up and data acquisition

The oil exploited in this experimental campaign is the Castrol Syntrans 75W-85 (around 4.5 l), which properties are listed in Table 2. In the table the fitting parameters (A,B) of the Andrade Equation (Eq. (1)) are reported. These parameters can be used to estimate the dynamic viscosity (μ) as a function of temperature (T). The fitting parameters B and A can be estimated according to Eqs. (2) and (3) respectively.
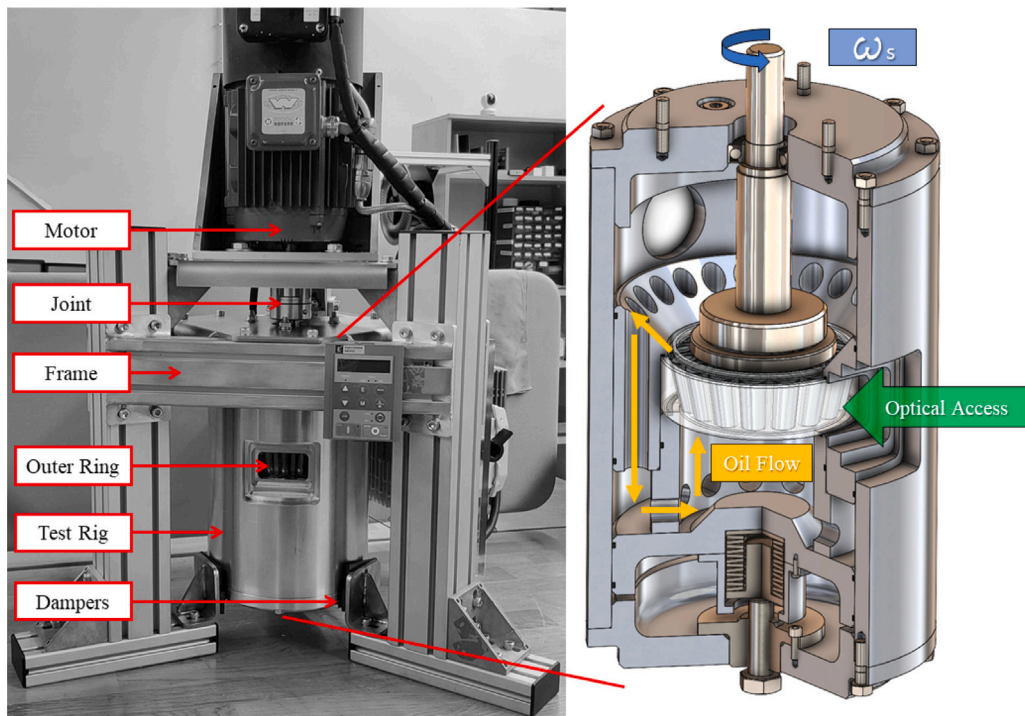
Fig. 1. Vertical Test Rig: assembly (left) and CAD model (right).

Table 2
Oil properties.

Symbol	Description	Value	Unit
ρ	Density	837	kg/m^3
$\mu_{40\ °C}$	Dynamic viscosity at 40 °C	54.07	mPa s
$\mu_{100\ °C}$	Dynamic viscosity at 100 °C	9.96	mPa s
$\nu_{40\ °C}$	Kinematic viscosity at 40 °C	64.6	mm^2/s
$\nu_{100\ °C}$	Kinematic viscosity at 100 °C	11.9	mm^2/s
A	Fitting parameter (coefficient) of the Andrade equation	367.76	Pa s
B	Fitting parameter (exponent) of the Andrade equation	0.028	K

The relation between the dynamic (μ) and kinematic (ν) viscosities is expressed by Eq. (4). This oil has been selected for two main reasons. First, it is an industrial oil that could actually be used for lubricating bearings. Second, in full-flooded lubrication, this oil allowed to avoid aeration even at high speeds.

$$\mu\,(T) = Ae^{B/T} \tag{1}$$

$$B = -ln\left(\frac{\mu_{40\ °C}/\mu_{100\ °C}}{40\ °C - 100\ °C}\right) \tag{2}$$

$$A = \mu_{100\ °C} \cdot e^{B\cdot(100+273)} \tag{3}$$

$$\nu = \frac{\mu}{\rho} \tag{4}$$

The oil has been seeded with 10 μm fluorescent polystyrene particles. Indeed, fluorescent PIV approach has been exploited to avoid noise in presence of the metallic surfaces of cage and rollers. In addition, it has to be pointed out that the steel cage in the target domain (Fig. 2) has been polished for avoiding any deposition of particles in its pores. In the present research, the velocity fields have been studied through a stereoscopic approach (two cameras) by using a LaVision's FlowMaster PIV system. The experimental set up is shown in Fig. 3. The cameras were arranged at a relative angle of 60° in the horizontal plane and inclined by an angle of 78° with respect to the vertical axis. These angles provide the best configuration for minimizing optical distortions while maximizing focus on the entire depth of the domain (Target Domain in Fig. 2). The lenses of the cameras are 105 − *mm* and the distance

from these lenses and the target domain is around 250 mm. Due to this distance, the entire target domain has been captured, maximizing the resolution of the scanning. The cameras are 14 bit Imager Pro X 4M with 2048 × 2048 pixel^2 sensor size, and 7.4×7.4 μm^2 pixel dimension. To avoid the noise of the fluorescent light capturing the fluorescent particles, camera lenses have been equipped with low-pass filters.

The laser exploited was an EverGreen 200 dual-cavity having a maximum pulse energy of 200 mJ and 532 nm of wavelength. Light-sheet forming optics have been installed on the laser to generate a 15 mm vertical light sheet to illuminate the target domain. In this case, the maximum depth of the measured domain coincides with the distance between the outer race and the cage. This volume is centered between two rollers, and includes regions in proximity to the rollers themselves (Fig. 2). In Fig. 2, the domain highlighted with a dot-dashed blue line coincides with the target domain studied in previous studies [5,6]. It is possible to notice that in the present study the target domain (highlighted with a yellow continuous line in Fig. 2) has been expanded in order to capture also secondary flows closer to the rollers.

The position of the cameras and the laser with respect to the test rig have been managed through a system of linear motion guides having perpendicular axes on which cameras and laser have been mounted. The calibration process was performed through a specific device which allows inserting a 3D calibration plate (LaVision 2-level plate with modified dimension) inside a sapphire outer ring (having the same dimension than the tested one), completely filled with the tested oil. In addition, the calibration device allows the plate to be positioned at the same inclination as the cage (12° with respect to the bearing axis), at
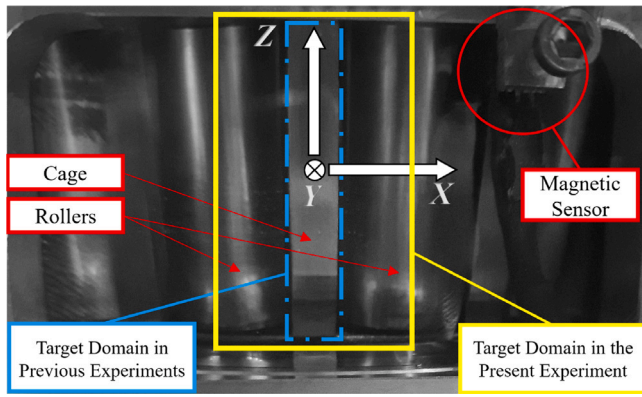
Fig. 2. View of the target domain for principal and secondary flows, magnetic sensor for synchronization, and (X, Y, Z) reference system.
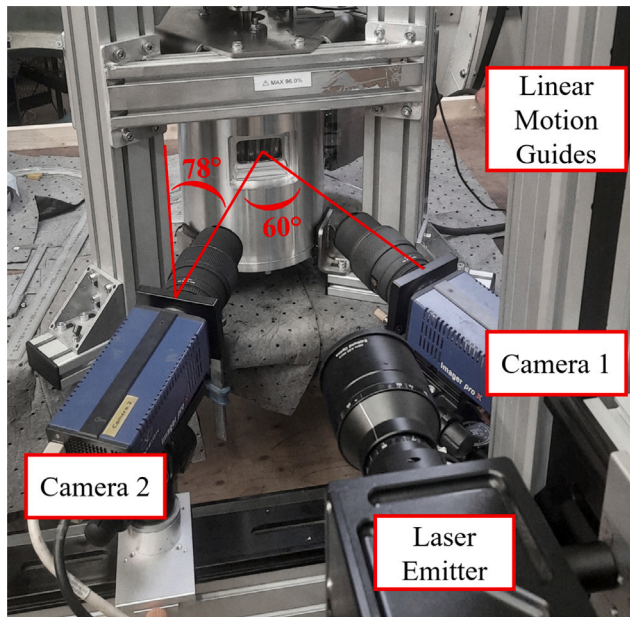

Fig. 3. Experimental set up for stereoscopic measurements.

Table 3
Investigated rotational speeds (ω_S), related inter-frame times dt, average cage velocities U_{X0}, monitored temperatures (T), and evaluated kinematic viscosities (ν).

ω_S	dt	U_{X0}	T	ν
min^{-1}	μs	m/s	°C	mm^2/s
500	180	1.14	26	96.4
1000	90	2.28	28	91.1
1500	60	3.42	31	83.8
2000	45	4.56	43	59.7
2500	36	5.70	45	56.5

magnetic trigger has been exploited. To this respect, a magnet has been applied to the cage and a magnetic Hall effect sensor was positioned on the outer part of the sapphire ring (see Fig. 2). The above-mentioned devices have been circumferentially positioned in order to generate the trigger signal when the target domain is located slightly upstream of the calibrated zone (Fig. 2). Through a specific setting of the time delay between the trigger and the image recording, it has been possible to fining-tune the PIV acquisition system at different rotational speeds.

The above-mentioned trigger has allowed evaluating the average rotational speed of the cage. The observed and the theoretical rotational speed of the cage (calculated based on the rotational speed of the shaft) differ for less than 0.5%. This evidence confirms the correctness of the kinematic of the bearing (ensured by the applied axial load). During the acquisition, each camera captured 100 dual image frames, i.e. two images acquired with a time difference dt (the so called inter-frame time) at each revolution of the cage for 100 rotations. This means that, every time that the magnet passes in the proximity of its magnetic sensor and, therefore, the target domain that is fixed with the cage is in the calibrated volume, each camera acquire two images at a specific inter-frame time. This process have been performed 100 times since the experimentation was set for 100 cage rotations.

The dt has been modified according to the rotational speed of the shaft (ω_S) to obtain the best signal-to-noise ratio of the final velocity fields. This was achieved with the inter-frame times shown in Table 3. The dt for different rotational speeds was set to have the maximum particle shift between the frames lower than 1/3 of the interrogation window size. The shaft speed was varied from 500 min^{-1} to 2500 min^{-1}, (Table 3). It is worth emphasizing that this maximum speed had never been achieved before in this type of experiment. Contextually, the oil temperature (T) was monitored and the average cage velocity (U_{X0}) (i.e. the speed measured at half its height) is also reported. Eventually, the estimated ν at the operating temperature is reported the last column of Table 3.

4. Numerical approach

A CFD model has been implemented in OpenFOAM®. The vertical orientation of the test rig allows exploiting the cyclic symmetries of the system. Indeed, gravity acts axially and, therefore, only a single sector of the TRB was modeled in this study. The sector in question involves cyclic symmetries passing through the center of two neighboring rollers. The computational domain has been discretized through the utility *blockMesh*. In this way, the mesh presents exclusively hexahedral cells. More specifically, the mesh properties are listed in Table 4.

The volume modeled with *blockMesh* is just half of the sector, the complete model has been created with a mirroring operation. The final model is shown in Fig. 4. In the figure, the "Shaft" group/patch (in dark blue) represents all the components having the rotational speed of the shaft, i.e. Shaft and Inner Ring. The "Outer Ring" group/patch (in white) represents all the components having a null velocity, i.e. Outer Ring and stationary components of the test rig (included a channel that allows the return of oil from the upper chamber to the lower chamber of the test rig). The Cage is indicated in green and the Rollers in red. Two cyclic Arbitrary Mesh Interfaces (AMIs) have been applied to the lateral

a controllable distance from the outer race. In this way, the calibration plate could be positioned in the middle of the target domain. This allowed creating a local reference system (X, Y, and Z) to decompose the measured velocity into its two in plane components (U_X and U_Z). More specifically, the U_X component is the one along the tangential direction (positive sign according to the cage rotation direction) while the U_Z component is the one along the vertical direction (positive according to the expected pumping effect, Fig. 2.

To perform the calibration process, the following steps are required. First, the calibration device has to be positioned in a dedicated structure. Then, through the linear motion guides, the cameras have to be positioned with respect to the calibration device according to the distances mentioned above. After the calibration, the cameras have to be moved in front of the target domain of the test rig with the same relative position. The calibration process has been improved over previous studies because markers were used on both the test rig and the calibration device. These markers facilitated an accurate positioning of the cameras relative to the aforementioned components.

Another challenge in performing PIV measurements in TRB is the synchronization between the camera and the cage. Indeed, cameras have to capture images in the target domain whose reference system is related to the cage rotation. To perform the synchronization, a
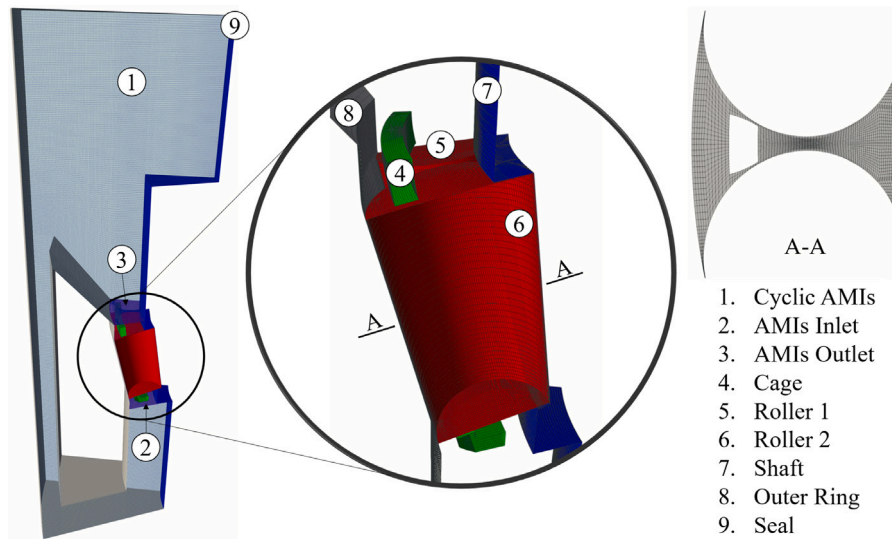
Fig. 4. Mesh and patches of the 32312-A model.

Table 4
Summary of the mesh quality parameters.

Quality parameters	Value
Cells total	2,019,612
Points total	2,116,918
Faces total	6,155,304
Internal faces	5,962,368
Max cell openness	4.54E−16
Max aspect ratio	95
Average non-orthogonality	9.83
Max skewness	1.7

Fig. 5. Kinematic of a Tapered Roller Bearing.

faces to model the cyclic symmetry of the test rig. Additional AMIs ("AMIs Inlet" and "AMIs Outlet" respectively) have been applied in the upper and lower part of the sector to simplify the modeling of the mesh outside the bearing. A very small patch has been created between the shaft and the frame to simulate the seal capable to prevent oil leakage but not to withstand overpressure. On this patch the relative pressure has been set equal to zero. The gap between each roller, the inner ring and the outer ring has been created by scaling the roller relative to its center of gravity. A preliminary mesh- and gap-sensitivity studies have been conducted. In this preliminary study, both the value of the gap (0.1 mm, 0.05 mm, and 0.01 mm) and the number of cells discretizing the area near the gap (width of 0.15 mm, 0.3 mm, 0.5 mm) were varied by using 10 elements in the gap thickness. In this sensitivity study, the resultant forces on the rollers were measured. It was noted that the optimal gap is that of 0.05 mm, decreasing further does not lead to a significant increase in the forces on the roller. In addition, it was found that the best compromise between computation time and accuracy is obtained by using 5 elements in the thickness and cells of width 0.3 mm near the contact.

In the present study, bodies have been modeled as rigid, and therefore, EHL effects have not been considered. This can be justified by the fact that the flow rate across the gap is two orders of magnitude smaller than the axial flow in TRBs and then does not affect the objective of this study.

In the present study, a Rigid Mesh Motion (RMM) approach has been implemented [1]. This approach relies on a rigid motion of the mesh (a rotation of the bearing sector around the axis of the shaft). The mesh is moved with the same rotational speed of the cage (ω_C). In this way, the apparent forces are generated by the mesh movement.

The theoretical kinematic of a TRB is represented in Fig. 5. In particular, in the figure, the angle of contact (α), the mean diameter
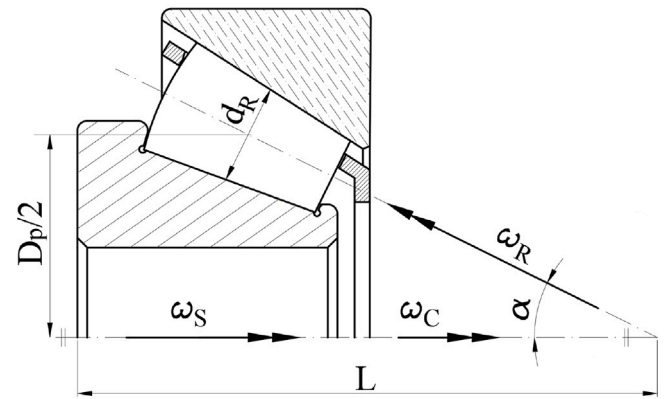
of the tapered roller (d_R), half the pitch diameter ($D_p/2$), the direction of the rotational speed of the Shaft (ω_S), the Cage ω_C, and the Roller ω_R are defined.

The rotational speed of the cage (and therefore of the mesh), and the pure rotational speed of the roller can be written as a function of the geometrical parameters (D_p, d_R, and α) and the input velocity ω_S according to Eq. (5) and Eq. (6) [42]. In these equations, it is implicitly considered that the outer ring has zero velocity.

$$\omega_C = \omega_S \frac{1}{2}\left[1 - \frac{d_R}{D_p}\cos(\alpha)\right] \tag{5}$$

$$\omega_R = \omega_S \frac{1}{2}\left\{\frac{D_p}{d_R}\left[1 - \left(\frac{d_R}{D_p}\cos(\alpha)\right)^2\right]\right\} \tag{6}$$

Since the mesh moves in space, it is possible to define the velocities of the boundaries in the local reference system (relative to the mesh sector) or in the global reference system (absolute). For example, in the local reference system, the velocity of the cage (ω_C^{rel}) can be set zero since the sector moves at the same velocity of the cage ω_C. Conversely, for simplicity, the velocity of the Outer Ring ω_{OR} and the Shaft ω_S can be set in the absolute reference system. In other words, the ω_{OR}^{abs} is set to zero while the ω_S^{abs} is equal to ω_S. These velocities could also be assigned in the relative reference system by subtracting the rotational speed of the mesh. The most complex kinematics is that of the Rollers, which required the development of a new
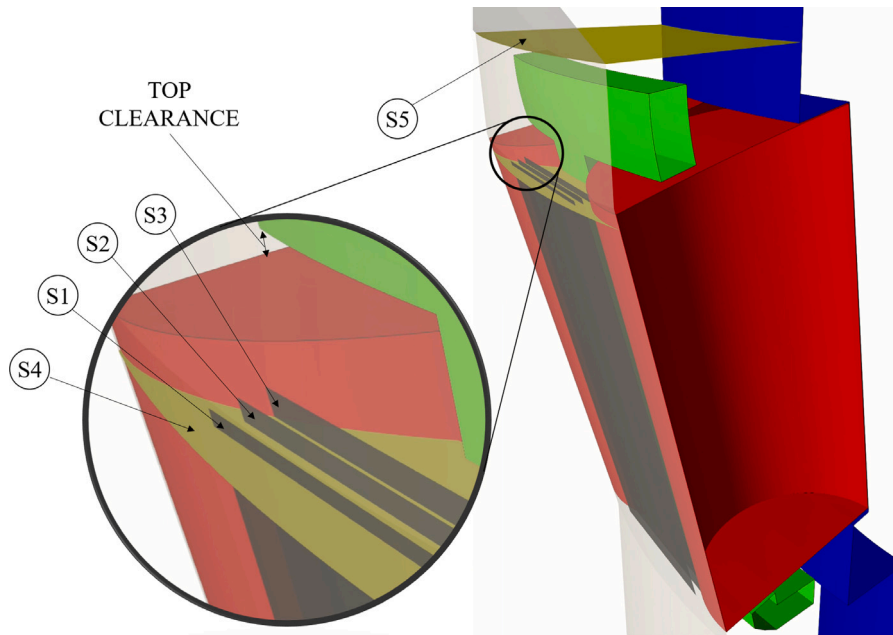
Fig. 6. Slices for post processing.

Table 5
Boundary conditions 32312-A.

Patch	U	p
Roller 1	$\omega_R^{rel} = \omega_R$	$\nabla p = 0$
Roller 2	$\omega_R^{rel} = \omega_R$	$\nabla p = 0$
Outer Ring	$\omega_{OR}^{abs} = 0$	$\nabla p = 0$
Shaft	$\omega_S^{abs} = \omega_S$	$\nabla p = 0$
Cage	$\omega_C^{rel} = 0$	$\nabla p = 0$
Seal	$\nabla U = 0$	$p = 0$
CyclicAMIs	*cyclicAMI*	*cyclicAMI*
AMIs Inlet	*cyclicAMI*	*cyclicAMI*
AMIs Outlet	*cyclicAMI*	*cyclicAMI*

U - velocity; p - relative pressure.

boundary condition in OpenFOAM® called "conicalWallVelocity" [6]. This boundary condition locates the axis of the Rollers in the absolute reference system and adds pure rotation velocities due to ω_R to the pure translation velocities caused by the motion of the Mesh. Therefore, the "conicalWallVelocity" boundary condition accurately reproduces the velocity field on each Roller, considering both rotation about its axis (with ω_R) and rotation about the bearing axis (with ω_C). The boundary applied conditions are summarized in Table 5.

Simulations have been performed setting the Courant (Co) number to $Co < 1$ in order to guarantee the numerical stability and convergence. A transient, single-phase, incompressible, laminar, and isothermal solver has been exploited. The stabilization of the fluxes have been reached in around two complete revolutions of the cage (two revolutions of the mesh). Therefore, simulations were stopped after two revolutions of the cage. By parallelizing the simulations on a High Performance Computing (HPC) Cluster AMD EPYC 7232P 16-Core Processor at 3.10 GHz (198.4 GFLOPs) the completion of two revolutions of the cage was achieved in around 15 h of computation time for each simulation.

Taking into consideration the average cage velocity at $\omega_S = 2500$ min^{-1}, i.e. $U_{X0} = 5.70$ m/s ($\nu = 56.5$ mm/s^2), and considering the characteristic length as the distance between the Cage and the Outer Ring (5 mm) (i.e. the flow is mainly tangential), it is possible to calculate the Reynolds number ($Re = 504$). Therefore, the laminar flow hypothesis can be justified. However, due the complexity of the flows present in the target domain, some additional simulations

including the Shear Stress Transport (SST) $k - \omega$ turbulence model have been performed at ω_S equal to 2000 min^{-1} and 2500 min^{-1}. This particular turbulence model offers an improved treatment near the wall by automatically switching between a wall function and a low-Reynolds number formulation based on the grid spacing. It is widely recognized that SST $k - \omega$ exhibits excellent performances when applied to flows around solid objects (i.e. presence of wall boundaries), and low Reynolds numbers. Exploiting the same hardware and end-of-simulation criteria, turbulent simulations took about 40% longer in comparison with laminar simulations.

Eventually, in order to compare the numerical results with the experimental ones, the CFD outcomes have been processed as follows. First, three slices (S1, S2, and S3), parallel to the calibration plate have been created (planes S1, S2, and S3 in Fig. 6). On these planes, the steady-state velocity values obtained from the CFD simulations have been interpolated. The final result has been obtained by averaging the fields on the three slices. In this way, the experimental (PIV) setup has been modeled and numerically reproduced. Second, in order to calculate the flow rate, slices S4 and S5 were created (Fig. 6). Through S5, it is possible to evaluate the total flow rate. Through S4, it is possible to calculate the external flow rate, i.e. axial flows that passed through the area between the cage and the outer race. It is interesting to notice that the PIV measurement allowed to estimate the external flow rate only.

5. Results and discussion

5.1. Experimental results

The ensemble-average has been obtained exploiting LaVision PIV processing software Davis 10. For each dual frame, the velocity vectors have been elaborated with the multi-pass PIV processing algorithm resulting in a final interrogation window size of 64×64 pixel^2 and 75% of overlapping. In Figs. 7 and 8 the velocity fields of decomposed in the tangential (U_X), and axial (U_Z) directions respectively are reported. The above-mentioned velocities have been scaled with respect to the scalar value average cage velocity (U_{X0}). In this way, it is possible to compare the measures for different ω_S. In addition, it is possible to notice that the range of the color scale (blue to red) is 0 to 1.5 for the U_X/U_{X0} and -0.5 to 0.5 for U_Z/U_{X0}. Eventually, it is worth
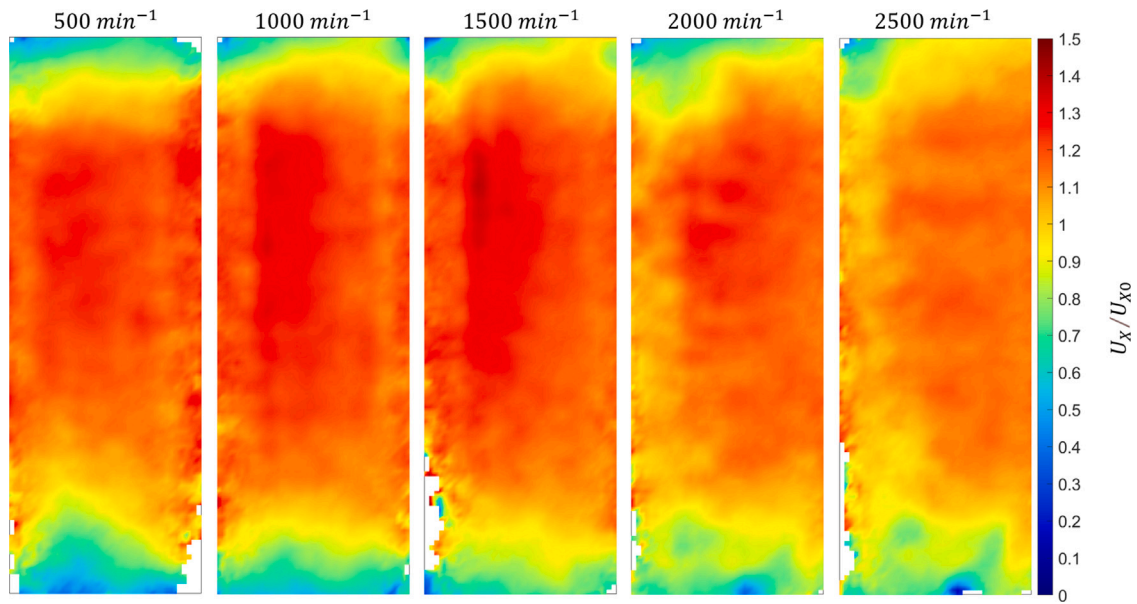
Fig. 7. Tangential velocity field (U_X) normalized with respect to the average cage velocity (U_{X0}) for different rotation speeds ω_S.
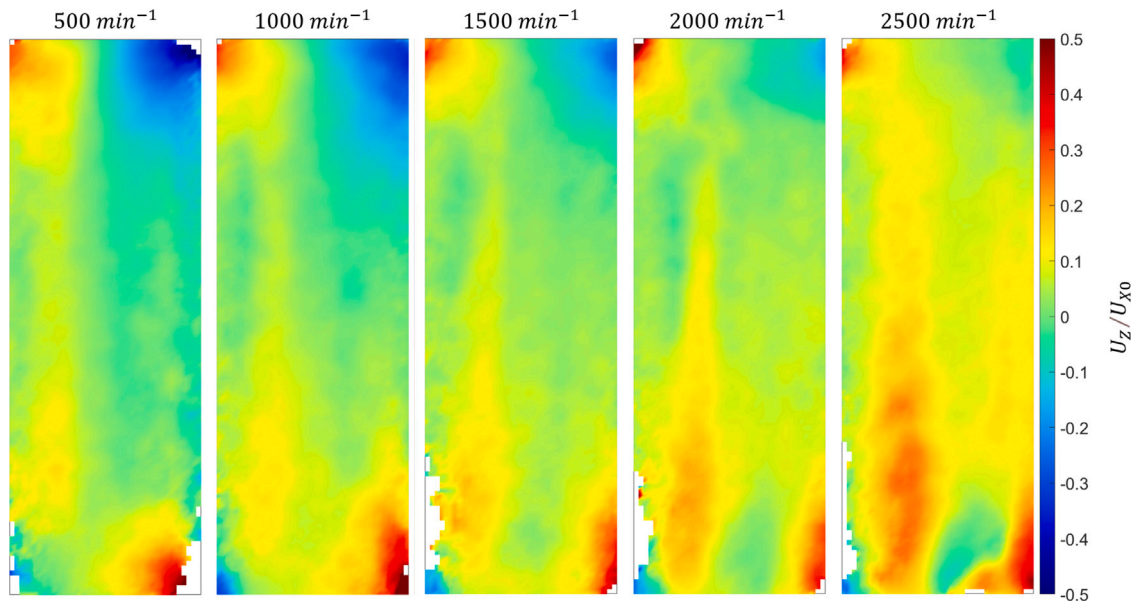

Fig. 8. Axial velocity field (U_Z) normalized with respect to the average cage velocity (U_{X0}) for different rotation speeds ω_S.

mentioning that, differently from previous experimental campaigns where the oil Nyflex 2014b was exploited, in the present experimental campaign, where Castrol Syntrans 75W-85 was used, no aeration was observed for the tests conducted in full-flooded lubrication.

Observing the results presented in Fig. 7, with regard to tangential velocities (U_{X0}), it can be seen that:

- The upper and bottom areas of the target domain show lower tangential velocities than the central part.
- The tangential velocities achieved in the central part of the target domain exceed the average cage speed ($U_X/U_{X0} > 1$).
- As ω_S increases, the difference between the average cage tangential velocity and the oil velocity tend to decrease and the maximum oil speed is shifted towards the right side of the target domain (the cage is rotating to the right).
- By increasing ω_S, turbulent effects seem to appear.

In Fig. 8 the axial velocity fields are reported. These are caused by the pumping effect of the TRB. It is very interesting to notice that, especially for low rotational speeds, positive and negative peaks occur in the corners of the target domain. More specifically, it appears that high positive axial velocities (i.e. caused by the pumping effect) occur in the upper left and lower right corners while high negative axial velocities (i.e. backward fluxes) occur in the opposite corners. This can be explained through the edge effect of the roller. Indeed, the left-hand roller carries an overpressure in the target domain while the right-hand roller carries a depression. The depression tends to draw flow from the upper and lower chambers into the target domain while the high pressure zones tend to eject oil from the target domain into the aforementioned chambers. These overpressure and depression are located close to the contact between the rollers and the outer race. In addition, the experimental measurements shows that as ω_S increases, the negative axial velocities tend to disappear from the target domain and positive axial velocities tend to increase more consistently.
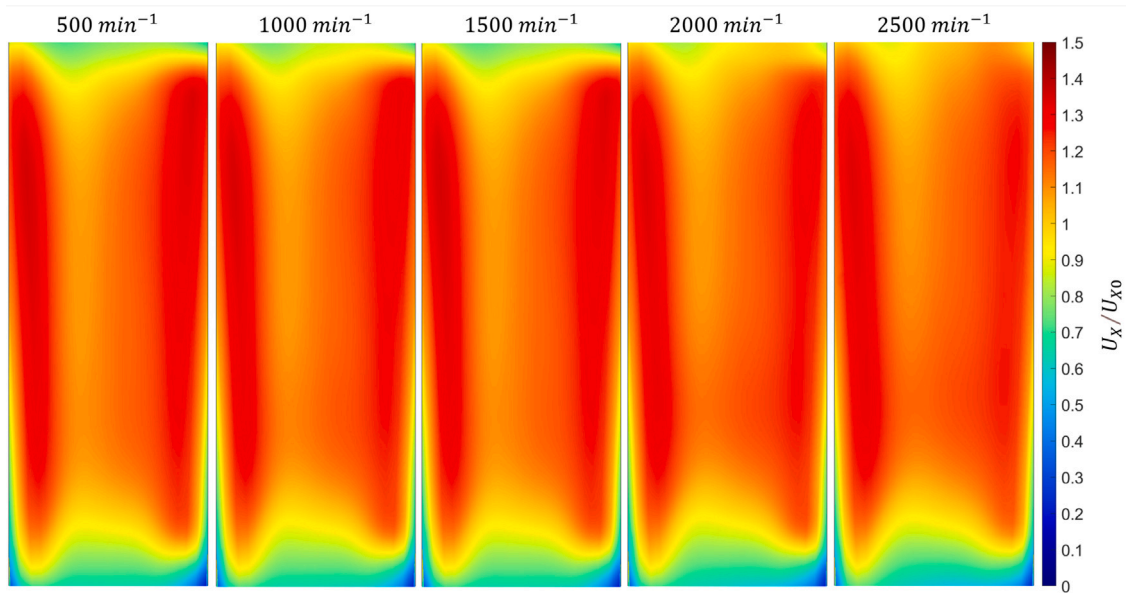
Fig. 9. Tangential velocity field (U_X) scaled with respect to the average cage velocity (U_{X0}) for different rotation speeds ω_S obtained with the laminar model.
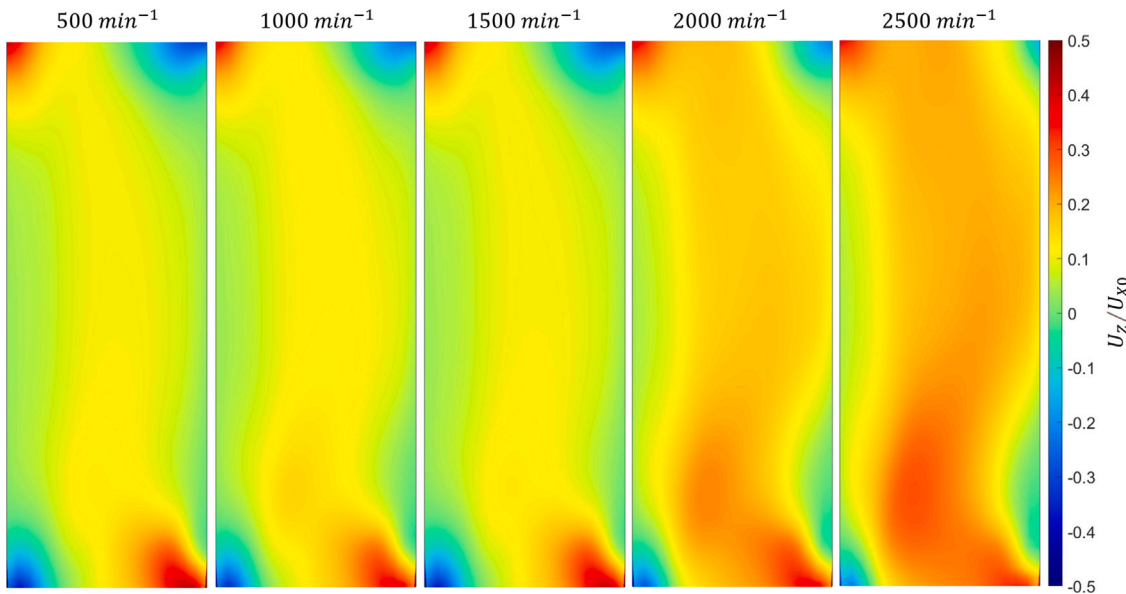

Fig. 10. Axial velocity field (U_Z) normalized with respect to the average cage velocity (U_{X0}) for different rotation speeds ω_S obtained with the laminar model.

Eventually, through the PIV measurements, it has been possible to roughly estimate the external flow rate. In other words, the average axial velocity (U_Z) can be multiplied for the cross sectional area (e.g. S4). The results can be compared with the numerical ones and are discussed at the end of the next section.

5.2. Numerical results

In Figs. 9 and 10 the tangential (U_X) and axial (U_Z) velocity fields scaled with respect to U_{X0} for different ω_S are reported. These results refer to modeling the flow as laminar. As anticipated in Section 4, results are the averaged values obtained in Slices S1, S2, and S3 (Fig. 6). The comparison between Figs. 9 and 7 leads to the identification of many similarities between experimental and numerical results. For instance, in both cases the fluid reaches tangential velocities higher than U_{X0}. Nevertheless, in the PIV measurements the higher velocities are more evenly distributed while in the numerical results, obtained with

the laminar model, they are slightly more skewed towards the rollers. In addition, the gradients present in the upper and lower zones of the domain are very similar in terms of shape and values. Eventually, in the numerical simulation results, as in the experimental measurements, as rotational velocities increase, the tangential velocity is relatively lower, especially near the right-hand roller.

The comparison between Figs. 10 and 8 shows an excellent agreement between experimental and numerical results. In particular, it is possible to notice that, in both cases, there is an area where the axial velocity increases. This region expands as the velocity increases. In addition, at lower rotational speeds the higher and lower velocities are positioned in the specific corners of the observed domain. The CFD confirmed that this effect is due by the high pressure gradients in the proximity of the contact between the roller and the outer race (see Fig. 11). In Fig. 11, it is possible to see both the distributions of relative pressures (p) on the Rollers and Cage surfaces and the velocity field on a series of slices. The results are in agreement with tangential
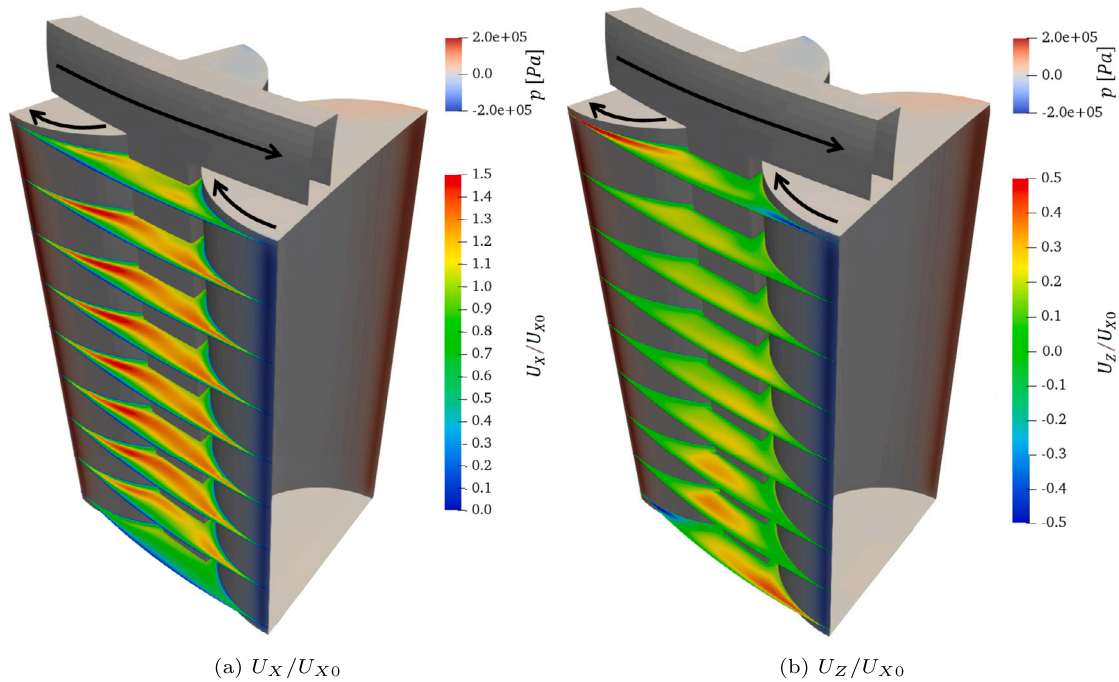
Fig. 11. Relative pressures distribution (p [Pa]) on roller and cage walls and colored slices in accordance with U_X/U_{X0} (a) and U_Z/U_{X0} (b) for $\omega_S = 2500$ min^{-1} obtained with the laminar model.

velocity (Fig. 11a) and axial velocity (Figs. 11b). These results refer to the laminar model at $\omega_S = 2500$ min^{-1}. Similar gradients can be observed closer to the contacts between rollers and inner race.

As mentioned in Section 4, simulations implementing SST $k - \omega$ turbulence model were completed to better understand whether the laminar flow assumption may be inappropriate in the target domain. Indeed, observing the experimental results at high velocities (Figs. 7 and 8), it is possible to glimpse a more diffuse velocity field probably due to an early turbulent transition. The results of the CFD simulations implementing SST $k - \omega$ turbulence model, in terms of U_X/U_{X0} and U_Z/U_{X0} for 2000 min^{-1} and 2500 min^{-1}, are shown in Fig. 12. To better appreciate the differences between the two CFD models (turbulent and laminar) and experimental observations, in Fig. 12, the numerical results of laminar simulations and those obtained experimentally for the above-mentioned rotational speeds in terms of tangential and axial velocity fields are reported.

The comparison highlights that, especially for what concerns the axial field, the turbulent simulations lead to closer results with respect to the experimental evidence. The differences between the two numerical approaches seem to be less significant in terms of tangential velocities. In any case, the PIV results seems to be in between the laminar and the turbulent predictions. In light of these differences, the comparison was made also considering the flow rates. More specifically, the flow rate passing through S4 and S5 (Fig. 6) allowed to estimate the external flow rate and the total flow rate respectively. In Fig. 13 the above-mentioned fluxes, together with the external flow rate measured via PIV, are reported for different rotational speeds.

It can be noticed that the external flow rate (the flow rate that passes through the volume inspected via PIV) measured via PIV and estimated via laminar CFD shows an excellent agreement especially for high rotational speeds. This leads to further confirmation of the laminar CFD model's ability to predict lubricant behavior. In addition, an interesting result that can be observed d Fig. 13 is that, contrary to Leibensperger's hypothesis [29], the external flow rate does not coincide with the total flow rate in the case of full-flooded lubrication of TRBs. Indeed, for low rotational speed ($\omega_S = 500$ min^{-1}) the external flow rate is the 54% of the total flow rate while for high rotational speed ($\omega_S = 2500$ min^{-1}) the share between external and total flow rate

achieve a value of 67%. This means that, by increasing the rotation speed, the percentage of the external flow rate becomes increasingly higher. Moreover, CFD simulations permitted to estimate the flow rate between the head of the roller and the cage (top clearance in Fig. 6). It is interesting to notice that, especially for low velocities, up to 25% of the total flow rate pass through that area (for high velocities this flow is about 5%). Therefore, from the external part of the cage there is always 75% to 80% of the total flow rate.

While the laminar CFD results coincide with the experimental ones, the turbulent CFD outcomes result significantly lower confirming that even at $\omega_S = 2500$ min^{-1} the flux is not fully turbulent but still in a transition regime. With these premises, and considering the increase in the computational effort to include a turbulence model, the results of this study seem to confirm the adequacy of the laminar approach for modeling such kind of conditions.

Eventually, it should be highlighted that the temperature, and therefore the viscosity, of the oil are not the same for the different measured and simulated conditions. This also justifies the irregular trends shown in Fig. 13. Indeed, as the rotational speed increased, the monitored operating temperature was increasingly higher (See Table 2).

6. Conclusions

In the present paper, an experimental study has been conducted to measure the velocity field in the external zone (i.e. the volume between the cage, rollers and outer race) of a TRB through the PIV technique. In this respect, a specific test rig with an outer ring made of sapphire has been used to allow the optical access to the inside of the bearing. Castrol Syntrans 75W-85 has been exploited as a lubricant in this experimental campaign and the full-flooded lubrication conditions without aeration have been ensured. Measurements have been performed at various rotational speeds up to the record speed of 2500 min^{-1}. Through the PIV measurements, it has been possible to characterize the velocity field in its axial and tangential components and to evaluate the external flow rate, i.e., the flow of lubricant involved by pumping effect in the external zone. During the experimental tests, the temperature has been monitored in order to estimate the properties of the oil through analytical equations. The experimental conditions have been reproduced
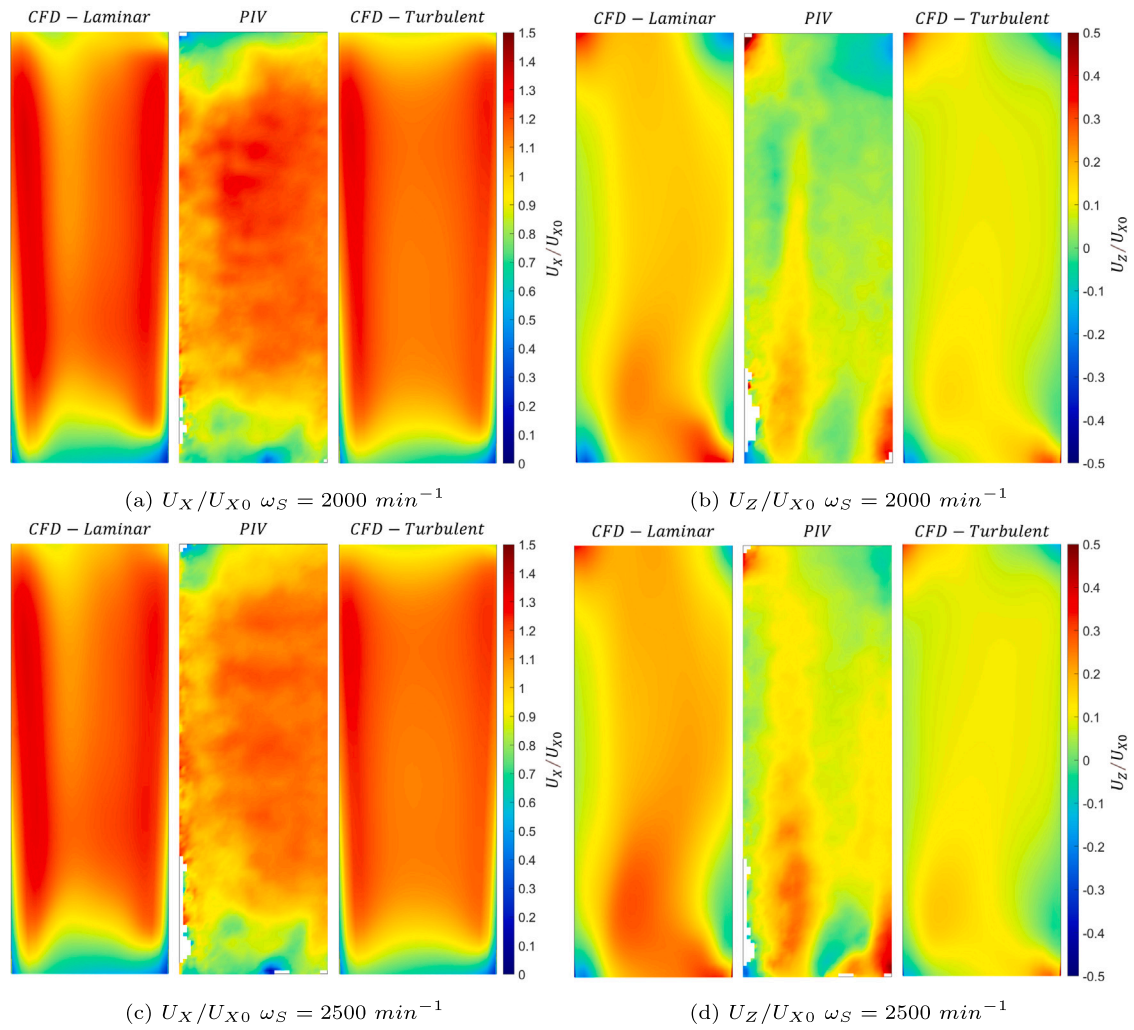
(a) U_X/U_{X0} $\omega_S = 2000$ min^{-1}

(b) U_Z/U_{X0} $\omega_S = 2000$ min^{-1}

(c) U_X/U_{X0} $\omega_S = 2500$ min^{-1}

(d) U_Z/U_{X0} $\omega_S = 2500$ min^{-1}

Fig. 12. Comparison between experimental (PIV), CFD exploiting laminar model, and CFD implementing SST $k-\omega$ in terms of U_X/U_{X0} (a, c) and U_Z/U_{X0} (b, d) for $\omega_S = 2000$ min^{-1} (a, b) and $\omega_S = 2500$ min^{-1} (b, c).
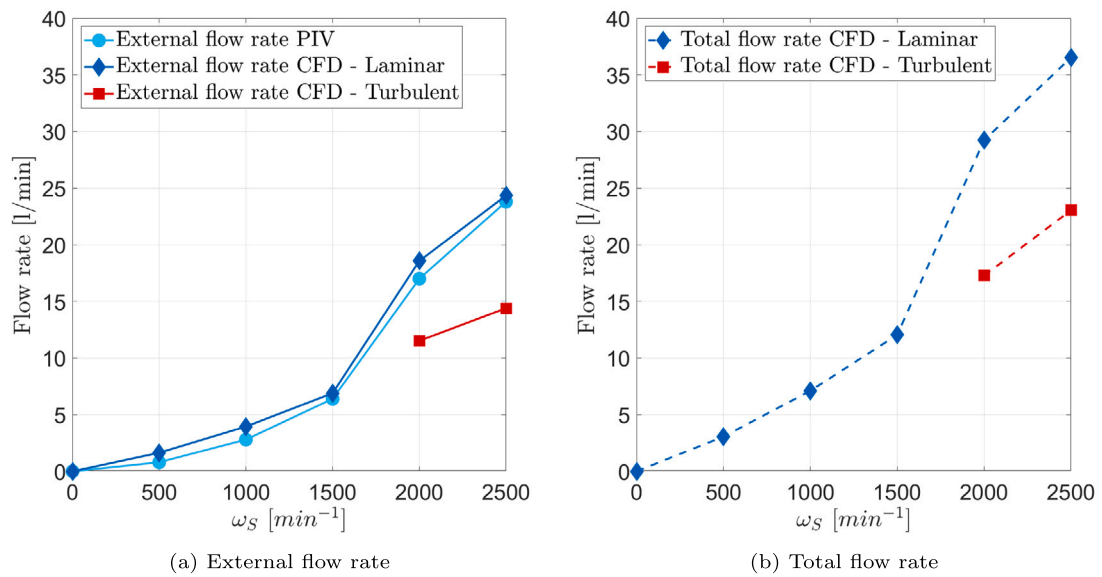

(a) External flow rate

(b) Total flow rate

Fig. 13. External flow rate measured via PIV and CFD (a) and Total flow rate estimated via CFD (b).

numerically in the OpenFOAM® environment. A simplified model of the test rig has been realized through a structured mesh. The numerical model includes a single sector (between two rollers) and exploits the cyclic symmetries of the system by implementing the RMM approach. Two single phase, isothermal models have been developed, i.e. laminar and turbulent (SST $k-\omega$). The simulations have been parallelized on 16 processors on an HPC Cluster AMD EPYC 7232P and stopped after two complete cage revolutions, when the flows have stabilized. By imposing an adjustable time step and setting the maximum Courant number equal to one, each simulation has been completed in around 15 h of computation time (for the laminar model), and around 21 h (for the turbulent one).

The turbulent model proved to be capable of capturing some details in the secondary flows more accurately than the laminar one. However, the turbulent model was shown to underestimate axial flow rate and required more computational effort. On the other hand, the laminar model showed an excellent ability to estimate the axial flow rate along with better computational performances. This may lead to the conclusion that the developed laminar model can be considered sufficiently accurate for the prediction of flows in TRBs subjected to full-flooded lubrication conditions. Certainly, for higher speeds turbulent modeling will be indispensable. In addition, through this experimental and numerical study it has possible to find that:

- Under full-flooded lubrication conditions, the external flow rate corresponds from 54% of the total flow rate for low rotational speeds (500 min⁻¹) to 67% of the total flow rate for high rotational speeds (2500 min⁻¹). This means that, in the overall flow rate balance due to the pumping effect, the internal flow (i.e., fluxes passing between the shaft and cage) cannot be neglected, especially for low speeds.
- Through the clearance between the rollers top-head and the cage (top clearance) there is abundant flow at low speeds. This leads to more than 70% of the lubricant flow coming out of the external side of the cage. However, as could be seen experimentally and numerically, only a portion of this flow rate passed through the external part under study in this paper.
- With respect to the tangential oil velocity (U_X), it turned out there are large areas where the U_X is greater than the average cage velocity U_{X0}, leading to high radial velocity gradients in the observed zone. In addition, it has been found that as ω_S increases, the percentage difference between the average tangential velocity of the fluid (U_X) and that of the cage(U_{X0}) is smaller.
- In terms of axial velocity (U_Z), it has been possible to observe squeezing effects (i.e. pumping due to high-gradients of pressure) in the corners of the target domain (close to the contacts between rollers and outer race). This happens especially at low speeds and it is due to the motion of the rollers producing two areas of high and low pressure straddling the contact between the roller and outer race. Furthermore, this study showed that as velocity increases, the axial flow rate in the target domain also increases and generates an average raising in axial velocity. Thus suppressing the downward flows in the target domain.

The study presented in this paper is not exempted from limitations. First, the calculation of the external flow rate through PIV processing has uncertainties due to the calculation of the fluid passage section and the use of average velocities measured in a plane. Future studies will involve measuring the total flow through more classical measurement tools. Second, the simulations were considered isothermal. Naturally, in the real case, in the contact areas between the cage, shaft, and outer ring with the rollers there is a flash temperature rise. Future studies would aim to use thermal solvers to study the effect of local temperature variations on the velocity and pressure fields. Third, the study was conducted under full-flooded lubrication conditions. The latter are rarely used in industry. Future studies should deal with oil-bath lubrication conditions using two-phase solvers. Fourth, only lubricant flows were considered in the experimental campaign presented in this paper, and power losses were not measured. Future studies will be aimed at measuring load-independent power losses.

Nomenclature

P_L	Total power losses
P_{LB}	Load-dependent power losses in bearings
P_{LB_0}	Load-independent power losses in bearings
P_{LG}	Load-dependent power losses in gears
P_{LG_0}	Load-independent power losses in gears
P_{LS}	Power losses due to seals
P_{LX}	Power losses due to other components such as clutches and/or synchronizers
CFD	Computational Fluid Dynamics
TRB	Tapered Roller Bearing
PIV	Particle Image Velocimetry
AMI	Arbitrary Mesh Interface
RMM	Rigid Mesh Motion
HPC	High Performance Computing
EHL	Elasto-Hydrodynamic Lubrication
A, B	Fitting parameters of Andrade Equation
SST	Shear Stress Transport
$k-\omega$	Transport-equation model solving for kinetic energy k and turbulent frequency ω
Co	Courant Number
Re	Reynolds Number
μ	Dynamic viscosity
ν	Kinematic viscosity
ρ	Density
ω_S	Theoretical rotational speed of the Shaft
ω_C	Theoretical rotational speed of the Cage
ω_R	Theoretical rotational speed of the Roller
ω_{OR}	Theoretical rotational speed of the Outer Ring
ω_S^{abs}	Rotational speed of the Shaft in the absolute reference system
ω_C^{rel}	Rotational speed of the Cage in the relative reference system
ω_R^{rel}	Rotational speed of the Roller in the relative reference system
ω_{OR}^{abs}	Rotational speed of the Outer Ring in the absolute reference system
d_R	Mean diameter of the tapered roller
D_p	Pitch diameter of the tapered roller bearing
L	Distance between the main bearing shoulder and the intersection of the shaft and roller rotation axes
α	Angle between the shaft and roller rotation axes
U	Velocity field
U_Z	Axial velocity component
U_X	Tangential velocity component
U_{X0}	Average cage velocity

Funding

Declaration of competing interest

The authors declare that they have no known competing financial interests or personal relationships that could have appeared to influence the work reported in this paper.

Data availability

The authors do not have permission to share data.

References

[1] Maccioni L, Concli F. Computational fluid dynamics applied to lubricated mechanical components: Review of the approaches to simulate gears, bearings, and pumps. Appl Sci (Switzerland) 2020;10(24):1–29. http://dx.doi.org/10.3390/app10248810.

[2] Tijare V, Nagaraj S, Pandya M, Wang J. Computational fluid dynamics study of oil lubrication in ball and roller bearings. In: Proceedings of the 6th national symposium on rotor dynamics: NSRD 2019. Springer; 2021, p. 253–65. http://dx.doi.org/10.1007/978-981-15-5701-9_21.

[3] Peterson W, Russell T, Sadeghi F, Berhan MT, Stacke L-E, Ståhl J. A CFD investigation of lubricant flow in deep groove ball bearings. Tribol Int 2021;154:106735. http://dx.doi.org/10.1016/j.triboint.2020.106735.

[4] Zhu W, Zhu R, Tang X, Lu F, Bai X, Wu X, Li F. CFD-based analysis of oil and gas two-phase flow characteristics in double-row tapered roller bearings with different rib structures. Appl Sci 2022;12(3):1156. http://dx.doi.org/10.3390/app12031156.

[5] Maccioni L, Chernoray V, Bohnert C, Concli F. Particle image velocimetry measurements inside a tapered roller bearing with an outer ring made of sapphire: Design and operation of an innovative test rig. Tribol Int 2022;165. http://dx.doi.org/10.1016/j.triboint.2021.107313.

[6] Maccioni L, Chernoray V, Mastrone M, Bohnert C, Concli F. Study of the impact of aeration on the lubricant behavior in a tapered roller bearing: Innovative numerical modelling and validation via particle image velocimetry. Tribol Int 2022;165. http://dx.doi.org/10.1016/j.triboint.2021.107301.

[7] Raju K, Veettil MP, Ray S, Shi F. Needle roller bearing lubricant flow CFD simulations. SAE Tech Pap Ser 2013;26:0041. http://dx.doi.org/10.4271/2013-26-0041.

[8] Adeniyi AA, Morvan HP, Simmons KA. A multiphase computational study of oil-air flow within the bearing sector of aeroengines. In: Turbo expo: power for land, sea, and air, Vol. 56734. American Society of Mechanical Engineers; 2015, http://dx.doi.org/10.1115/GT2015-43496, V05CT15A024.

[9] Wu W, Hu C, Hu J, Yuan S. Jet cooling for rolling bearings: Flow visualization and temperature distribution. Appl Therm Eng 2016;105:217–24. http://dx.doi.org/10.1016/j.applthermaleng.2016.05.147.

[10] Hu J, Wu W, Wu M, Yuan S. Numerical investigation of the air-oil two-phase flow inside an oil-jet lubricated ball bearing. Int J Heat Mass Transfer 2014;68:85–93. http://dx.doi.org/10.1016/j.ijheatmasstransfer.2013.09.013.

[11] Zhang R, Wei C, Wu W, Yuan S. CFD investigation on the influence of jet velocity of oil-jet lubricated ball bearing on the characteristics of lubrication flow field. In: Proceedings of 2015 international conference on fluid power and mechatronics. 2015, p. 1324–8. http://dx.doi.org/10.1109/FPM.2015.7337326.

[12] Feldermann A, Fischer D, Neumann S, Jacobs G. Determination of hydraulic losses in radial cylindrical roller bearings using CFD simulations. Tribol Int 2017;113:245–51. http://dx.doi.org/10.1016/j.triboint.2017.03.020.

[13] Concli F, Schaefer C, Bohnert C. Innovative meshing strategies for bearing lubrication simulations. Lubricants 2020;8(4). http://dx.doi.org/10.3390/LUBRICANTS8040046.

[14] Mastrone MN, Hartono EA, Chernoray V, Concli F. Oil distribution and churning losses of gearboxes: Experimental and numerical analysis. Tribol Int 2020;151:106496. http://dx.doi.org/10.1016/j.triboint.2020.106496.

[15] Hartono EA, Golubev M, Chernoray V. PIV study of fluid flow inside a gearbox. In: PIV13; 10th international symposium on particle image velocimetry. Delft University of Technology, Faculty of Mechanical, Maritime and Materials Engineering, and Faculty of Aerospace Engineering; 2013.

[16] Ji Z, Stanic M, Hartono EA, Chernoray V. Numerical simulations of oil flow inside a gearbox by smoothed particle hydrodynamics (SPH) method. Tribol Int 2018;127:47–58. http://dx.doi.org/10.1016/j.triboint.2018.05.034.

[17] Massini D, Fondelli T, Andreini A, Facchini B, Tarchi L, Leonardi F. Experimental and numerical investigation on windage power losses in high speed gears. In: Turbo expo: power for land, sea, and air, Vol. 50886. American Society of Mechanical Engineers; 2017, http://dx.doi.org/10.1115/GT2017-64948, V05BT15A034.

[18] Richardson D, Sadeghi F, Rateick Jr RG, Rowan S. Using μPIV to investigate fluid flow in a pocketed thrust bearing. Tribol Trans 62(3).

[19] Yan K, Dong L, Zheng J, Li B, Wang D, Sun Y. Flow performance analysis of different air supply methods for high speed and low friction ball bearing. Tribol Int 2018;121:94–107. http://dx.doi.org/10.1016/j.triboint.2018.01.035.

[20] Aamer S, Sadeghi F, Russell T, Peterson W, Meinel A, Grillenberger H. Lubrication, flow visualization, and multiphase CFD modeling of ball bearing cage. Tribol Trans 2022;65(6):1088–98. http://dx.doi.org/10.1080/10402004.2022.2123420.

[21] Russell T, Sadeghi F, Peterson W, Aamer S, Arya U. A novel test rig for the investigation of ball bearing cage friction. Tribol Trans 2021;64(5):943–55. http://dx.doi.org/10.1080/10402004.2021.1953657.

[22] Noda T, Shibasaki K, Wang Q. X-ray ct imaging of grease behavior in ball bearing and multi-scale grease flows simulation. In: Society of Tribologists and Lubrication Engineers Annual Meeting and Exhibition 2016. 2016, p. 361–2.

[23] Noda T, Shibasaki K, Miyata S, Taniguchi M. X-ray CT imaging of grease behavior in ball bearing and numerical validation of multi-phase flows simulation. Tribol Online 2020;15(1):36–44. http://dx.doi.org/10.2474/trol.15.36.

[24] Mastrone MN, Concli F. CFD simulation of grease lubrication: Analysis of the power losses and lubricant flows inside a back-to-back test rig gearbox. J Non-Newton Fluid Mech 2021;297:104652. http://dx.doi.org/10.1016/j.jnnfm.2021.104652.

[25] Wen Y, Oshima S. Oil flow simulation based on CFD for reducing agitation torque of ball bearings. SAE Int J Passenger Cars - Mech Syst 2014;7(4):1385–91. http://dx.doi.org/10.4271/2014-01-2850.

[26] Santhosh R, Hee JL, Simmons K, Johnson G, Hann D, Walsh M. Experimental investigation of oil shedding from an aero-engine ball bearing at moderate speeds. In: Turbo expo: power for land, sea, and air, Vol. 50923. American Society of Mechanical Engineers; 2017, http://dx.doi.org/10.1115/GT2017-63815, V07AT34A018.

[27] Arya U, Peterson W, Sadeghi F, Meinel A, Grillenberger H. Investigation of oil flow in a ball bearing using bubble image velocimetry and CFD modeling. Tribol Int 2023;177:107968. http://dx.doi.org/10.1016/j.triboint.2022.107968.

[28] Gorse P, Dullenkopf K, Bauer H-J, Wittig S. An experimental study on droplet generation in bearing chambers caused by roller bearings. In: Turbo expo: power for land, sea, and air, Vol. 43147. 2008, p. 1681–92. http://dx.doi.org/10.1115/GT2008-51281.

[29] Leibensperger R. An analysis of the flow of oil through a tapered roller bearing. J Tribol 1972;94(2):125–30. http://dx.doi.org/10.1115/1.3451652.

[30] Zhou R, Hoeprich M. Torque of tapered roller bearings. J Tribol 1991;6:590–7. http://dx.doi.org/10.1115/1.2920664.

[31] Liebrecht J, Si X, Sauer B, Schwarze H. Investigations of hydraulic losses in in tapered roller bearings [Untersuchungen von hydraulischen Verlusten an Kegelrollenlagern]. Tribol Schmierungstech 2015;62(3):14–21.

[32] Liebrecht J, Si X, Sauer B, Schwarze H. Investigation of drag and churning losses on tapered roller bearings. Strojniski Vestnik/J Mech Eng 2015;61(6):399–408. http://dx.doi.org/10.5545/sv-jme.2015.2490.

[33] Liebrecht J, Si X, Sauer B, Schwarze H. Technical-mathematical approach for the calculation of the flow and churning losses in tapered roller bearings [Technisch-mathematischer Ansatz zur Berechnung der Plansch- und Strömungsverluste am Kegelrollenlager]. Tribol Schmierungstech 2016;63(4):5–13.

[34] Liebrecht J, Si X, Sauer B, Schwarze H. Consideration of the influence of size in the calculation of churning and drag losses on rolling bearings [Berücksichtigung des Größ eneinflusses bei der Berechnung der Plansch- und Schleppverluste an Wälzlagern]. Tribol Schmierungstech 2017;64(2):46–52.

[35] Gonda A, Großberndt D, Sauer B, Schwarze H. Experimental and numerical investigations of hydraulic losses in rolling bearings under practice-oriented conditions [Experimentelle und numerische untersuchungen der hydraulischen verluste in Wälzlagern unter praxisrelevanten Bedingungen]. Tribol Schmierungstech 2018;65(6):7–13.

[36] Gonda A, Sauer B, Großberndt D, Schwarze H. Experimental and numerical investigation of hydraulic losses in rolling bearings. In: STLE 2019 - 74th annual meeting and exhibition of the society of tribologists and lubrication engineers. Nashville, Tennessee, USA; 2019.

[37] Gonda A, Sauer B, Großberndt D, Schwarze H. Experimental and numerical investigations of hydraulic losses in fully and partially fluted, tapered roller bearings [Experimentelle und numerische untersuchungen der hydraulischen verluste in voll-und teilgefluteten kegelrollenlagern]. VDI-Ber 2019;2019(2348):97–106.

[38] Hirt C. Modeling turbulent entrainment of air at a free surface. Flow Science, Inc; 2003.

[39] Brecher C, Fey M, Bartelt A, Hassis A. Design and test rig experiments of a high speed tapered roller bearing for main spindle applications. Procedia Cirp 2016;46:533–6. http://dx.doi.org/10.1016/j.procir.2016.04.053.

[40] Zhou X, Zhu Q, Wen B, Zhao G, Han Q. Experimental investigation on temperature field of a double-row tapered roller bearing. Tribol Trans 2019;62(6):1086–98. http://dx.doi.org/10.1080/10402004.2019.1649509.

[41] Roshchin V. Experimental estimation of energy losses in tapered roller bearings. Russian Aeronaut 2020;63:111–6. http://dx.doi.org/10.3103/S106879982001016X.

[42] Majdoub F, Mevel B. Kinematic equilibrium of rollers in tapered roller bearings. Tribol Trans 2019.